Sensor Malfunction Detection and Mitigation Strategy for a Multilevel Photovoltaic Converter

Armin Teymouri, Graduate Student Member, IEEE, and Ali Mehrizi-Sani, Senior Member, IEEE

Abstract—Cascaded H-bridge (CHB) based converters have several advantages including modularity, isolated DC-side voltage, and improved output voltage quality. These multilevel converters are increasingly used in photovoltaic (PV) systems. With the number of H-bridge submodules (SM) and sensors increased due to the cascaded topology, the converter becomes more prone to sensor malfunctions. This paper proposes a method to make a CHB-based PV converter resilient to sensor malfunctions using a real-time state estimation—based malfunction detection algorithm. The proposed method is validated using simulation studies in MATLAB/SIMULINK and experimental studies on a test system. It is shown that a nine-level CHB-based PV system can operate normally even when one sensor measurement is missing.

Index Terms—Malfunction detection, multilevel converter, power electronics, sensor malfunction, solar energy.

I. Introduction

THE AVERAGE worldwide cost of large-scale PV units has dropped 75% from 2010 to 2017 to 40 cents per watt [1]. The total installed solar power capacity in the U.S. reached 47 GW in July 2017, which equals the power needed to supply more than 9 million American homes [2]. The ongoing increase in the integration of solar PV units inevitably increases the impact of their malfunctions on the power grid [3], [4].

A PV system malfunction can have several reasons, e.g., sensor loss or cyber attack. A malfunction in a large-scale PV unit has an impact similar to a solar eclipse. While a solar eclipse has a predictable pattern and typically the needed regulatory reactions are arranged, a malfunction is not predictable. During the 2017 eclipse in the U.S., an estimated 1900 utility-scale solar plants were affected [5], and the reserve units provided the needed power with a ramp rate of 150 MW/min [6]. Without preparations, the grid would have probably collapsed [6].

The growing integration of large-scale PV units necessitates more reliable power electronic converters [7]. CHB-based converters are a potential solution for interfacing PV units to the grid [8]. Their advantages include modularity, isolated DC-side voltage, decreased switching losses due to a low switching frequency, increased output voltage quality, and submodule-level maximum power point tracking (MPPT) [9]. There are more sensors in a CHB-based converter than a conventional voltage-sourced converter (VSC). This increases the vulnerability of a CHB-based converter to sensor malfunctions [3].

However, there are no studies addressing the vulnerability of power electronic converters and particularly CHB-based topologies to sensor malfunctions.

There is ample research performed on the stability and unbalanced operation of CHB-based PV inverters. Reference [10] proposed an MPPT algorithm that can track the MPP for each module independently and deal with strict power mismatch conditions. A novel converter topology is introduced in [11] that can alleviate the power mismatches between the modules of different phases. The general solution for the power imbalance problem is the injection of zero sequence currents and voltages. Reference [12] provides a review on different methods to address instabilities in CHB-based PV systems. Among all the different methods, increasing the system resiliency to sensor malfunctions is not studied.

There are efforts to reduce the number of sensors in a CHB-based converter. A sensorless PWM algorithm based on a converter topology with a reduced number of switches is analyzed in [13]. Most of the topologies that have a reduced component count are developed using hybrid converter topologies [14]–[16]. Modifying the MPPT algorithm is another way for reducing the component count and removing the sensors in a CHB-based converter [17]. A 19-level CHB-based PV system without a DC-side current sensor is proposed in [18]. Several efforts to perform MPPT without using current sensors on the DC-side are reported in [17], [19]-[22]. Reference [23] develops a method to eliminate both the voltage and current sensors on the DC-side of a CHB-based converter. Reference [24] increases the power conversion efficiency in a multilevel inverter by reducing the number of switches. Reference [25] provides a review of the modular power electronics solutions with reduced switch count. However, to the best of the authors' knowledge, none of these studies focuses on detecting a malfunctioning sensor and making a CHB-based converter resilient to sensor malfunctions.

While reducing component count and sensors in a CHB-based PV system has several advantages [13], it decreases the modularity and redundancy of the system. It may also complicate the topology and controllers. This paper proposes a method to increase the redundancy of a CHB-based PV system and make it more resilient to sensor malfunctions. This paper does not eliminate sensors in the system; rather, it proposes an algorithm that enables the system to operate normally when a sensor is lost. A state estimator unit calculates the system variables independently of the sensors health status. This paper also develops an algorithm to detect the malfunctioning sensor and replace its measurement with an accurate estimate. A nine-level CHB-based PV system is utilized to evaluate

1

A. Teymouri is with the School of Electrical Engineering and Computer Science, Washington State University, Pullman, WA, 99164 USA (e-mail: armin.teymouri@wsu.edu).

A. Mehrizi-Sani is with the Bradley School of Electrical and Computer Engineering, Virginia Polytechnic Institute and State University (Virginia Tech), Blacksburg, VA, 24061 USA (e-mail: mehrizi@vt.edu).

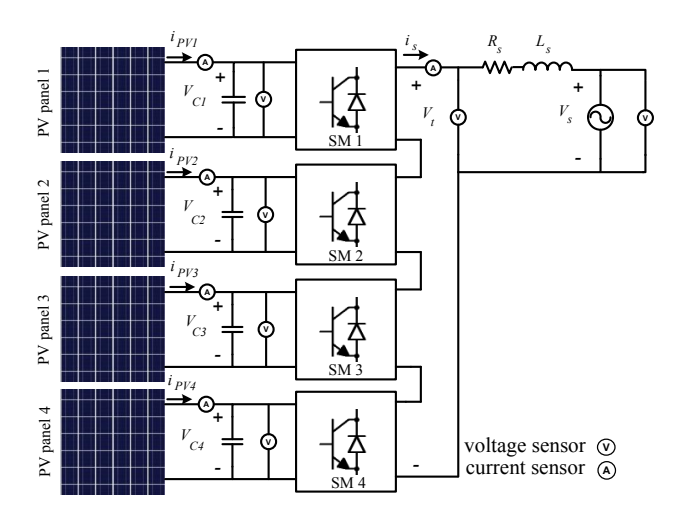


Fig. 1. Nine-level CHB-based PV study system.

the proposed algorithms. Different sensors are subjected to malfunctions and the performance of the system is analyzed using MATLAB/SIMULINK and experimental results.

The contributions of the paper are

- Method to estimate the measurements,
- Sensor malfunction detection scheme,
- Switching scheme for CHB-based converters that have malfunctioning sensors, and
- CHB-based PV system resilient to sensor malfunctions.

The remainder of this paper is organized as follows. Section II discusses the study system. The proposed estimation method is discussed in Section III. Section IV discusses the proposed sensor malfunction detection algorithm. Section V evaluates the validity of the proposed algorithms by simulation and experimental results. Section VI concludes the paper.

II. CHB-BASED PV STUDY SYSTEM

Fig. 1 shows the topology of a nine-level CHB-based PV system with four SMs. Each SM has an independent MPPT algorithm. The MPPT and the switching algorithms need measurements of the DC-side voltage and current. Therefore, there are 8 sensors on the 4 DC buses of this topology. The AC side has 3 sensors: AC-side terminal voltage V_t , the AC-side current i_s , and the grid voltage V_s . There is also a DC-side voltage V_C and a DC-side current i_{PV} sensor for each SM.

The control block diagram of the converter is shown in Fig. 2. Two loops control the flow of the d- and q- axis currents. The parameters of the PI controllers are $K_p=0.2$ and $K_i=0.02$. The MPPT algorithm determines the reference DC voltage for the control loop controlling the reference d-axis current i_d . The output voltage is controlled using reactive power.

This paper assumes that the instantaneous output voltage of an individual SM cannot be zero. As will be discussed in Section III, this is because the estimation algorithm needs the modulation index M, which is a continuous value between -1 and 1 shown in (1), to be nonzero. To guarantee this, at each moment, the output of one SM is decided based on PWM while the other three SMs generate either V_C or $-V_C$.

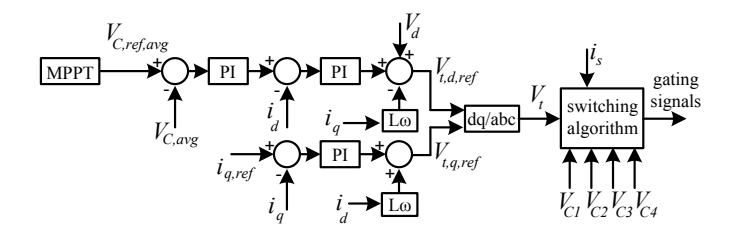


Fig. 2. Block diagram of the CHB-based converter controller.

The modulation index for the SM that is in PWM mode is calculated as follows:

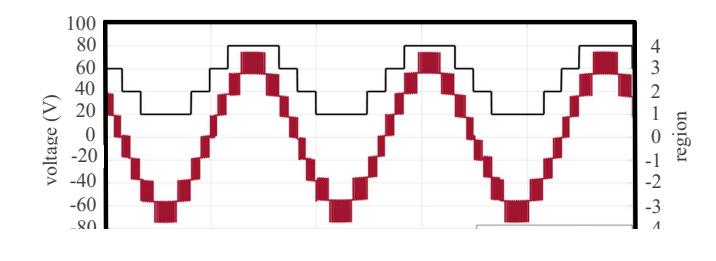
$$M_{\text{PWM}} = \frac{V_{t,ref} - \sum_{i=1, i \neq \text{PWM}}^{n} (M_i V_{C,i})}{V_{C,\text{PWM}}},$$
 (1)

where V_t is the output terminal voltage, and V_C is the DC-side voltage. The output of the current controller is compared with the average DC-side voltage to define 4 different switching regions. The number of regions in the switching schemes with zero as an output for individual SMs is 8 [26], [27]. This reduction from 8 to 4 in the number of regions in this paper simplifies the switching algorithm. It reduces the number of switching states and the memory used in the controller. Thus, it lowers the calculation burden of the controller. Furthermore, the number of SM switchings and the switching loss decrease. This reduction is even more pronounced in CHBs with higher number of levels.

The proposed switching states for an n-level CHB-based converter are shown in Table I, in which M_h is the modulation index for the SM with highest V_C , M_n is for the module with lowest V_C , and M_i to M_m are for other modules. The SMs that have the highest capacitor voltages should be discharged first and those with the lowest voltages should be charged first. Fig. 3 shows the terminal voltage of the nine-level CHB-based PV system. At each voltage level, one SM works in PWM mode. This helps the terminal voltage track its sinusoidal reference more accurately. At each switching region in Table I, if an SM is detected to have a sensor malfunction on its DC-side sensors, the estimation algorithm discussed in Section III prevents it from working in the PWM mode; thus, its switching scheme changes to faulted mode as shown in Table I. The SMs are sorted based on the amplitude of their DC-side voltages. When an SM in PWM mode is detected to have a sensor malfunction, PWM is performed by the SM with the next higher or lower voltage level, depending on the current direction and the charge or discharge needs.

III. PROPOSED ESTIMATION AND CALCULATION METHODS

To have a system resilient to sensor malfunctions, it is necessary to have alternative ways to obtain sensor measurements. The methods proposed in this paper to calculate each of the sensor measurement values are discussed in this section.



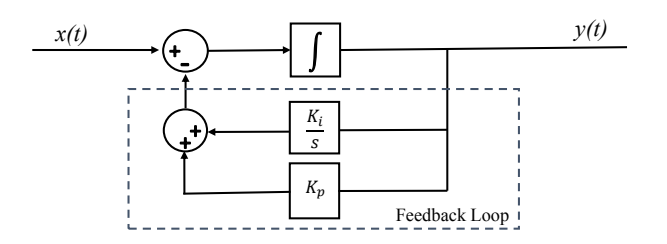


Fig. 4. Block diagram of the integrator with feedback loop.

A. Calculation of the Grid Voltage V_s

To calculate V_s , a KVL on the AC-side gives

$$V_{s,calc} = L_s \frac{di_s}{dt} + R_s i_s + \sum_{j=1}^{4} M_j V_{C,j},$$
 (2)

where R_s and L_s are the resistance and inductance of the AC-side filter, M_j is the modulation index for each SM, $V_{C,j}$ is the DC-side capacitor voltage, and i_s is the AC-side current of the converter. The grid voltage sensor is an important sensor. To lower the chances of this sensor malfunctioning, it is assumed that this sensor has a quality higher than the other sensors in system. However, it is possible to use a PLL to determine the grid voltage phase angle and update it in real time. A KVL on the AC side between the terminal and the grid voltage gives the amplitude of the grid voltage. The calculated amplitude can be used in (2) to detect if the grid voltage sensor is malfunctioning. If a malfunction is detected, the calculated amplitude and the recorded phase angle replace the malfunctioning measurement.

B. Calculation of the Output Current i_s

To calculate i_s , a KVL on the AC-side gives

$$i_{s,calc} = \frac{1}{L_s} \int_T (\sum_{j=1}^4 M_j V_{C,j} - R_s i_s - V_s) dt.$$
 (3)

Because of the DC value in this integral, it is necessary to develop an integrator with feedback, Fig. 4. This integrator has a PI controller in its feedback loop with parameters tuned such that the fundamental- and higher-frequency components are the same as an integrator without feedback.

The AC-side current i_s can also be calculated from the measurements of the DC sides of the individual SMs based on KCL. Since there are four SMs in the converter and the sensor measurements on each SM are independent of each other, it is

possible to estimate i_s from any SM. Equation (4) shows the second method to calculate i_s .

$$i_{s,calc,j} = \frac{1}{M_i} (i_{PV,j} - C_j \frac{dV_{C,j}}{dt}), \qquad j = 1, 2, 3, 4.$$
 (4)

As (4) shows, M cannot be zero. Based on the switching strategy shown in Table I, no more than one SM can work in the PWM mode at any given time. If an SM is in PWM mode, its modulation index can cause the denominator in (4) to be very small, and possibly zero. As a result, the estimated signal for the AC-side current can become inaccurate. Therefore, the estimate based on the SM in PWM mode is eliminated.

C. Calculation of the DC-Side Voltage V_C

The DC-side voltage V_C of each SM can be calculated as:

$$V_{C,j,calc} = \frac{V_t - \sum_{i=1, i \neq j}^4 M_i V_{C,i}}{M_j}.$$
 (5)

This method is independent of the DC-side currents.

D. Calculation of the DC-Side Current i_{PV}

 i_{PV} is calculated using a KCL at the DC-side of each SM:

$$i_{PV,j,calc} = C_j \frac{dV_{C,j}}{dt} + M_j i_s.$$
 (6)

E. Calculation of the AC-Side Terminal Voltage V_t

A KVL on the AC-side outputs of different SMs gives

$$V_{t,calc} = \sum_{i=1}^{4} M_i V_{C,i}.$$
 (7)

The output terminal voltage sensor is not usually installed in a commercial inverter. The proposed algorithm needs to use this sensor and it is added to the study system. This sensor measures the terminal voltage with a high bandwidth, based on the commercially available technologies [3].

IV. PROPOSED MALFUNCTION DETECTION SCHEME

Fig. 5 shows the flowchart of the AC-side current state estimator and detection algorithm. This paper considers only one sensor malfunction at a time. Only three SMs can provide estimates, as the fourth SM is in PWM mode and cannot be used for estimation. Step 1 in malfunction detection is the estimation of the AC-side current i_s from each of the SMs, Fig. 7(a). The spikes in Fig. 7(a) are created by the single SMs that are in PWM mode. To eliminate these spikes, at each time step, the 4 estimated currents are processed and merged into 3 signals and the one signal coming from the SM in PWM mode is removed, Fig. 7(b). In addition to these 3 estimates, the AC-side current can also be calculated using (4).

Step 2 is to calculate the average of these inputs, Fig. 7(c). Since a large bad value, which can be an estimate or a measurement, can shift the average, three-by-three average values, each leaving out one signal, are calculated. If a signal deviates from all the three-by-three averages, it is denoted as falsified. The deviation threshold ε is heuristically set to 5%.

 M_{PWM}

-1

 $i_{out} \ge 0$ $i_{out} \ge 0$ M_j M_k M_l M_m M_h M_i M_j M_k M_{l} M_m region 1 1 M_{PWM} 1 1 1 M_{PWM} region M_{PWM} -1 -1 region 1 region 1 1 M_{PWM} M_{PWM} -1 region 2 1 -1 region 2 M_{PWM} M_{PWM} -1 -1 -1 -1 region 1 region 1 M_{PWM} -1 $i_{out} < 0$ $i_{out} < 0$ M_h M_i M_i M_k M_l M_{r} M_n M_h M_i M_i M_k M_l M_n M_{*} M_{PWM} M_{PWM} region region -1 M_{PWM} region -1 M_{PWM} 1 region 1 1 1

 M_{PWM}

region 2

region 1

-1

 M_{PWM}

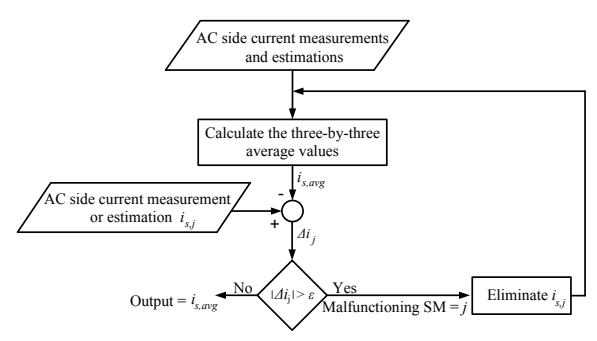
TABLE I PROPOSED SWITCHING SCHEME OF AN n-LEVEL CHB-BASED CONVERTER IN NORMAL AND FAULTED CONDITIONS.

Once the bad value is detected, step 3 is to eliminate it from the average calculation formula and calculate a new average. This process can continue until there is no wrong estimate left. However, this paper considers only one malfunction. The final average value can be used instead of the actual measurement of the AC-side current. If an estimate deviates from the average, its corresponding SM can be detected. Because the SM-based estimates of the AC-side current are calculated using the DC-side voltage and current measurements, the wrong i_s estimate is a result of a wrong measurement from either V_C or i_{PV} .

region 2 region 1

In step 4, (5) and (6) are used to determine if the malfunction is caused by V_C or i_{PV} . In both cases, a change should be made in the switching process of the detected SM. M can be zero in PWM mode and because there is a division by M in (5), this SM cannot work in PWM mode anymore. Therefore, its modulation index M is either +1 or -1. The proposed switching scheme during the loss of a DC-side sensor is shown in Table I. Since no more than one sensor is expected to malfunction in this paper and that sensor is already detected, the measurements from other SMs can be trusted. The measured V_C is compared with (5). If they are not equal, the measurement is considered to be wrong. If they are equal, the measurement is accurate and the accuracy of the DC-side current sensor needs to be checked. If the DC-side current measurement is not equal to (6), it is falsified. Thus, it should be replaced by its estimated value. Based on solver calculations, the proposed scheme reasonably increases the solver computational burden by 10%. However, the solver step size is the same for systems with and without the proposed algorithm.

Although this paper considers only one sensor malfunction at a time, the proposed method can also detect two sensor malfunctions on an SM at the same time. Based on (5), calculation of V_{DC} does not depend on the DC-side current of the same SM. Thus, malfunction detection of V_{DC} of an SM is independent of i_{PV} of that SM. If V_{DC} is detected to be malfunctioning, the value from (5) replaces the measurement in (6). Thus, (6) can be used to detect if the DC-side current sensor on that SM is malfunctioning. The proposed method can calculate and estimate the measurements and detect the malfunctions independently of the system conditions. For



-1

 M_{PWM}

Fig. 5. AC-side current state estimator and malfunction detection flowchart.

example, if there is a malfunction in the converter and the output terminal voltage becomes zero, the calculation for this measurement is also zero and matches the measurement. Thus, the proposed method does not confuse the malfunctions in sensors with malfunctions in other parts of the system.

V. SIMULATION AND EXPERIMENTAL RESULTS

This section evaluates the proposed algorithm on a ninelevel single-phase grid-connected CHB-based PV system using simulations and experimental studies. The topology of this system is shown in Fig. 1 and its experimental setup is shown in Fig. 6. The parameters of the system for the simulations and the experimental setup are the same, as shown in Table II. The electrical parameters of the system are chosen heuristically. Four 25 W PV panels are connected to the DC-sides of the SMs. This converter is connected to a 60 Hz grid with an rms voltage of 32 V, which is chosen to be lower than the terminal voltage of the PV converter in low insolation conditions. The experiments are performed on a small-scale system. However, the proposed method is fully scalable and is expected to work for a large scale system too. The proposed algorithm is implemented using an OPAL-RT real-time simulator and controller. The voltage and current sensor measurements are received by an I/O expansion unit and sent to OPAL-RT. The I/O unit receives the gating signals from the OPAL-RT and sends them to the converter. The converter utilizes SKM IGBT modules and SKYPER 32 R gate drivers. The utilized IGBT

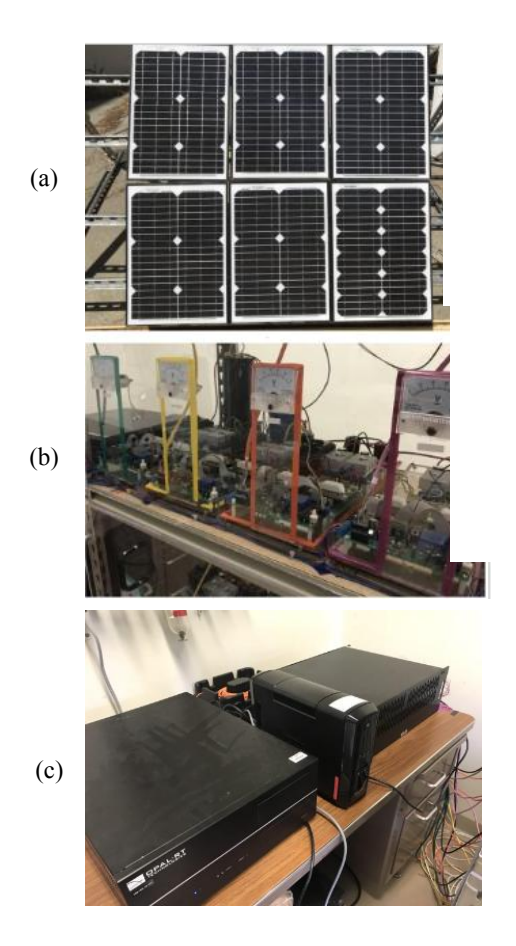


Fig. 6. The experimental setup for the proposed system: (a) PV panels, (b) CHB converter, (c) OPAL-RT and I/O unit.

 $\begin{tabular}{ll} TABLE & II \\ SIMULATION & AND & EXPERIMENTAL & SETUP & PARAMETERS. \\ \end{tabular}$

Electrical Parameters			
PV panel power	25 W	C_{DC}	15 mF
$V_{s,rms}$	32 V	L_s	7 mH
$f_{ m switching}$	2500 Hz	R_s	0.4 Ω
	Controller	Parameters	
Current Controller		Integrator Feedback	
K_p	1.5	K_p	0.1
$\dot{K_i}$	55	$\vec{K_i}$	0.5

modules can withstand up to 2.5 times the nominal AC-side current, which is 10 A. Different scenarios are discussed for simulation and experimental verifications. Subsections A-D discuss the simulation results. Subsections E and F present the experimental results while comparing them with a similar scenario using simulations.

A. Estimation of the AC-Side Current i_s

As mentioned previously, the estimate resulting from the SM in PWM mode is oscillatory and cannot be used. Fig. 7(a) shows the primary estimates of the AC-side current in normal operating condition. Fig. 7(b) shows the estimate results after eliminating the estimates from the SM in PWM mode and processing the 4 primary signals into 3. The oscillatory output of the estimated AC-side currents are removed and only negligible glitches are left. These glitches are eventually

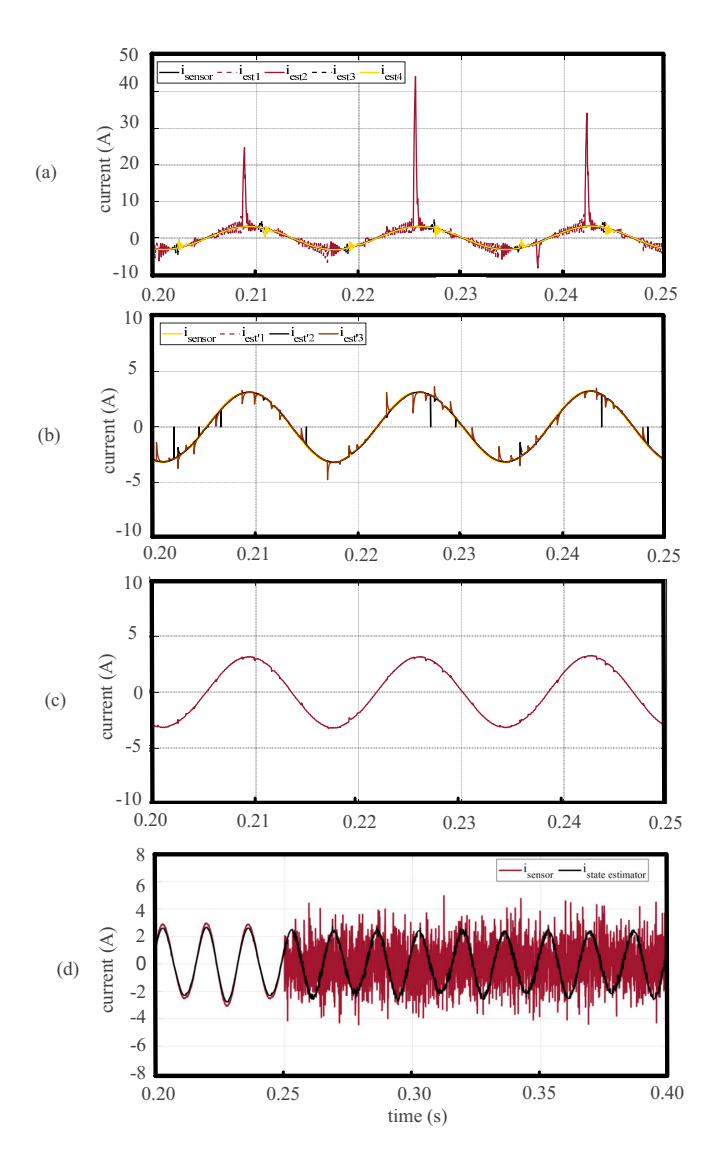


Fig. 7. The simulated AC-side current, (a) primary estimates, (b) estimates after eliminating the SM in PWM mode, (c) state estimation output; and (d) sensor and state estimation output with a sensor malfunction happening at $t=0.25~\rm s$.

removed by taking the average value of the estimates shown in Fig. 7(b).

The proposed algorithm also deals with bad measurements. The final value for the AC-side current used by the controllers is the mean value of all the estimates and the sensor measurement. If the sensor measurement is different from the mean value of the estimates, it is removed and a new value is calculated based only on the estimates. The output of the state estimation module is shown in Fig. 7(c). The signals shown in Fig. 7(a) and Fig. 7(b) are not used anywhere within the controllers and are shown only to illustrate the process of reaching to Fig. 7(c).

To show the performance of the detection algorithm, a sensor malfunction is introduced into the system that causes a white noise on the sensor measurement. Such faulty measurements can have different reasons such as the sensor being disconnected, a short circuit in sensor wiring, noise, or cyber attack. The detection algorithm detects and eliminates the bad data.

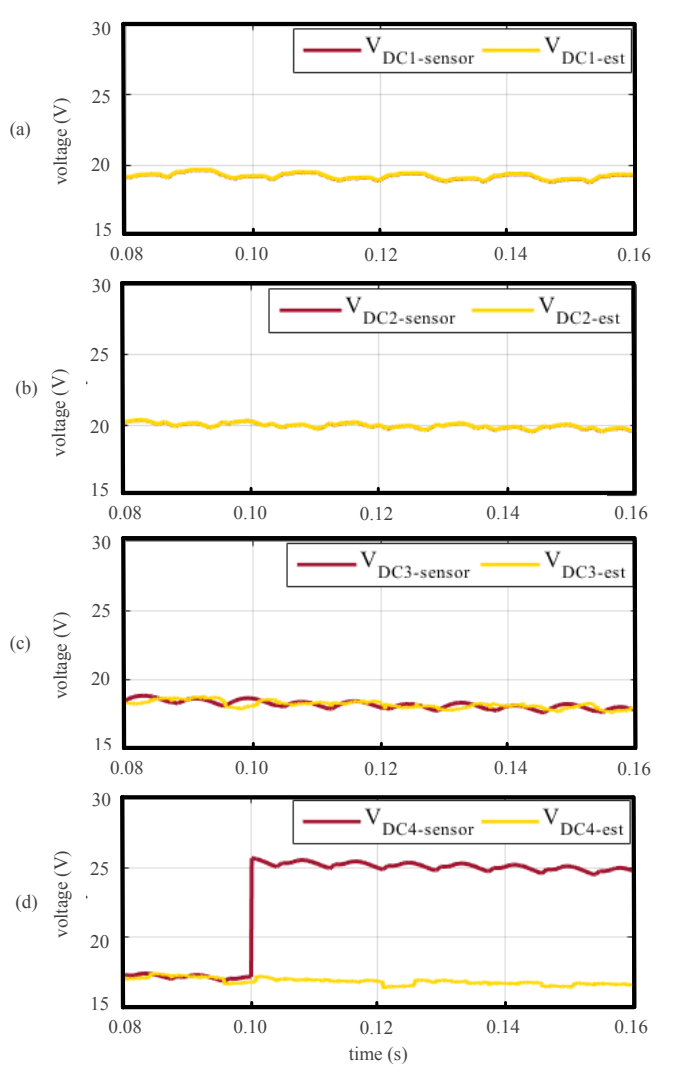


Fig. 8. Simulation results with a sensor malfunction happening in SM 4 at $t=0.10~{\rm s}_{10}$ (a)-(d) the outputs of the DC-side voltage sensors and calculations.

Fig. 7(d) shows the measurement and the state estimates output before and after the introduction time the malfunction.

B. Calculation of the DC-Side Voltage V_{DC}

Fig. 8 shows the measurements and calculations of the DC-side voltages. These voltages are not equivalent because of different insolation levels and MPPs. The calculations are accurate. If an SM is in PWM mode, the calculation for that SM is less accurate, but still within the acceptable range. At $t=0.10~\rm s$, the DC-side voltage of SM 4 is falsely measured. However, the estimate for this signal stays accurate. This malfunction is detected by the detection algorithm and the corresponding sensor is then blocked.

C. Calculation of the DC-Side Current i_{PV}

Figs. 9(a)–(d) show the calculation results for the DC-side currents. At $t=0.25~\rm s$, the measured DC-side current in SM 4 starts to malfunction. The sensor measurement is then replaced by the accurate calculation of this signal. The terminal voltage

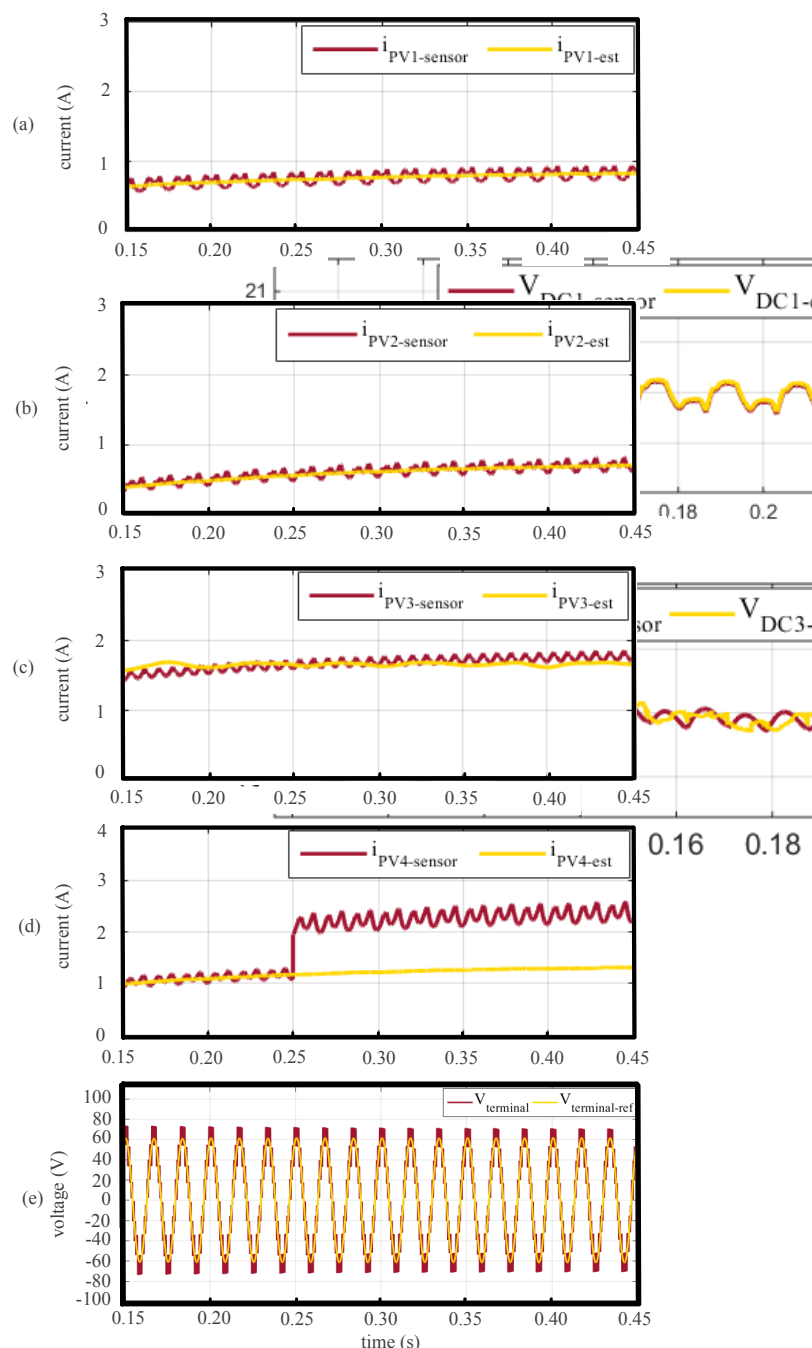
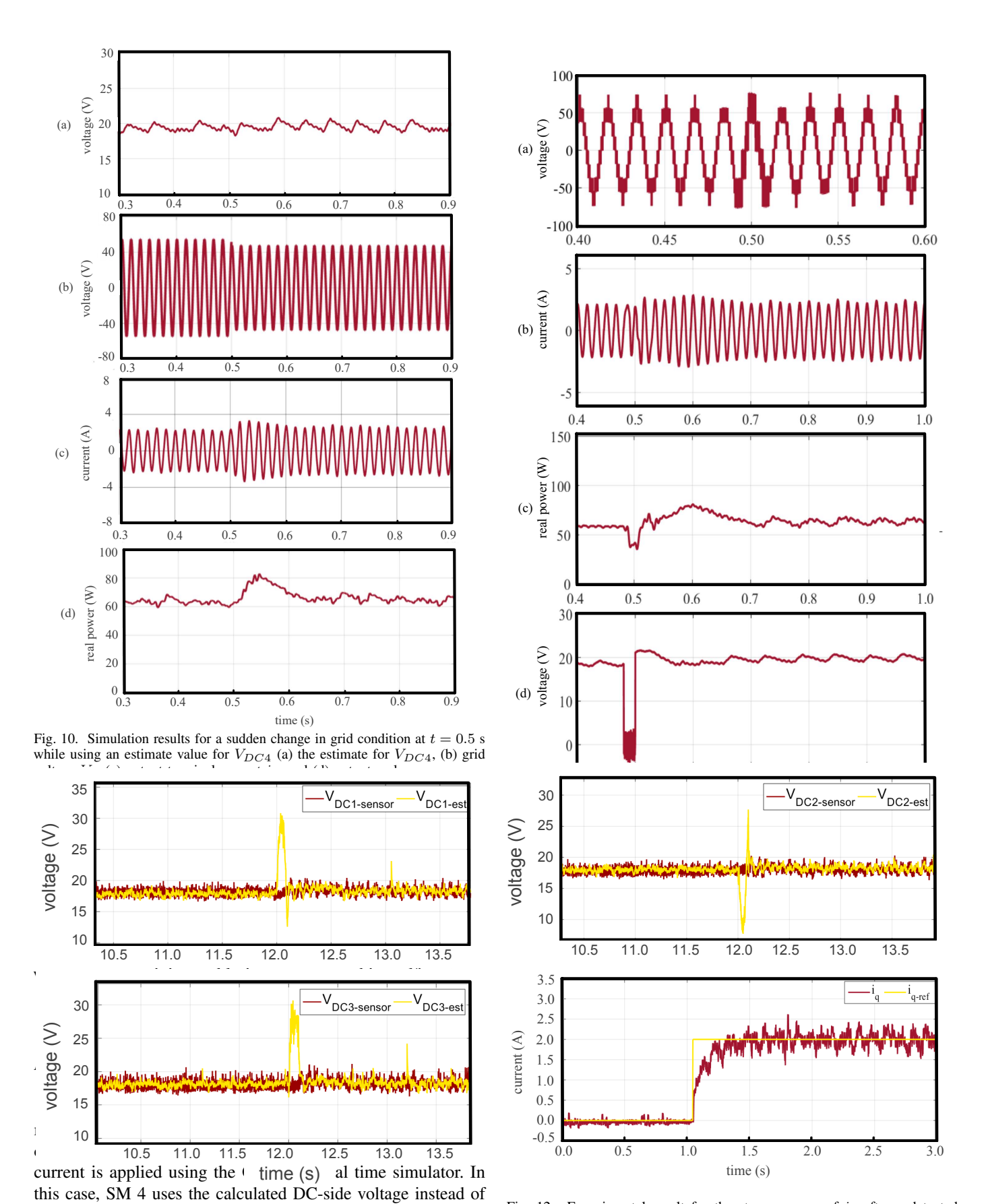


Fig. 9. Simulation results with a sensor malfunction happening in SM 4 at $t=0.25\,\mathrm{s}$ (a)-(d) The output of the DC-side current sensors and their calculated values, (e) terminal voltage and its reference.

of the converter and its reference value are shown in Fig. 9(e). The output terminal voltage is a nine-level staircase waveform superpositioned by a PWM waveform at each level.

D. Uncertain Grid Conditions after Losing a Sensor

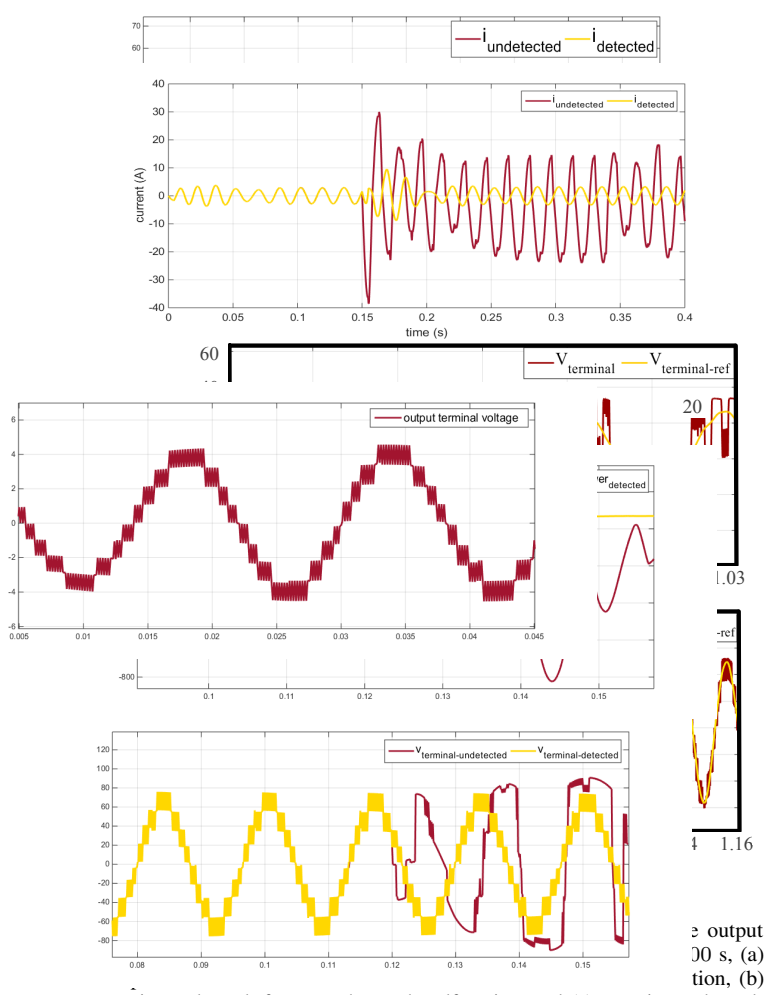
To evaluate the performance of the proposed system under uncertain grid conditions, after a sensor is lost, the grid experiences a 5% voltage drop at t=0.5 s. Fig. 10 shows the simulation results on how the steady state output power of



its measured value. The reactive current and its reference are

shown in Fig. 12. The system can accurately track the changes in reactive power set point after a sensor malfunctions

Fig. 12. Experimental result for the step response of i_q after a detected malfunction in the DC-side voltage sensor of SM 4.



experimental result for an undetected malfunction, and (c) experimental result for a detected malfunction.

F. Comparison of the Results of Detected and Undetected Malfunctions

This case study compares the system performance as a result of a detected and an undetected malfunction, first, via simulation and, then, experimental results.

In simulation, an error in the measurement of the DC-side voltage of SM 4 is introduced at $t=1\,\mathrm{s.}$ In this scenario, for the simulations, the resulting waveforms of the detected and undetected malfunctions are shown together in a same subfigure. Fig. 13(a) shows the simulated terminal voltage for both the detected and undetected malfunction. The detection and replacement of a falsified measurement by an accurate calculation helps the terminal voltage remain stable. Fig. 14(a) shows the simulated output terminal current as a result of a detected and undetected malfunction. Furthermore, an undetected malfunction causes the real power output of the converter to become negative. In a practical scenario, in an experimental setup, the protection system prevents such an out-of-bound negative value. However, as shown in Fig. 15(a), the real power remains unchanged if the malfunction is detected.

Under the same conditions as the detected and undetected simulated malfunctions in this section, the experimental setup is tested. The experimental results of the detected and undetected malfunctions for each wavefrom are shown in different subfigures. The first experimental scenario investigates the

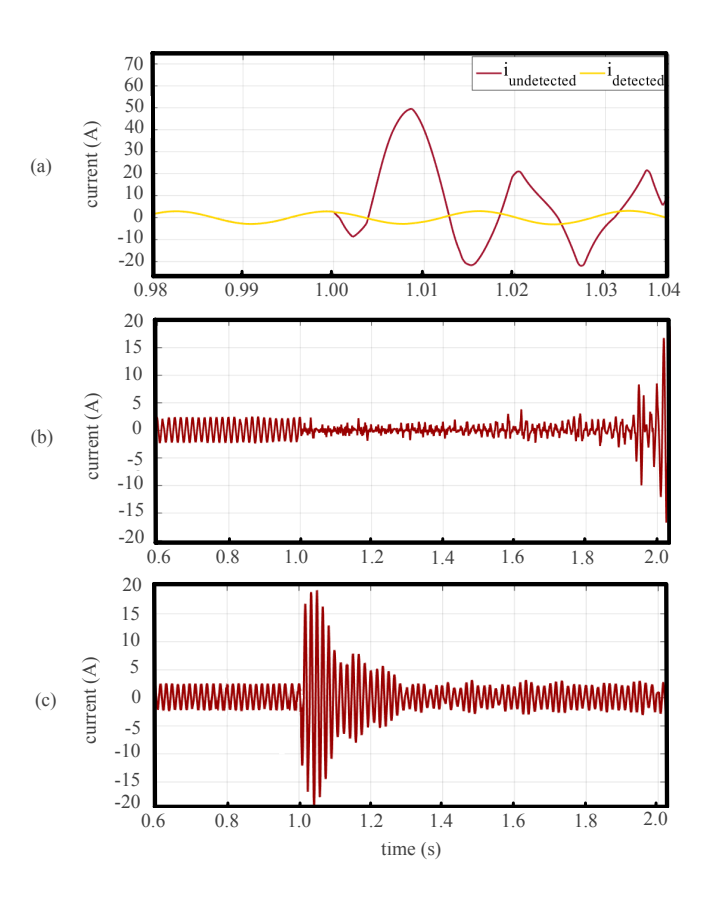


Fig. 14. Simulation ((a)) and experimental ((b),(c)) results for the output current with a malfunction happening on V_{DC4} at $t=1.00~\rm s$, (a) comparison of a detected and an undetected malfunction in simulation, (b) experimental result for an undetected malfunction, and (c) experimental result for a detected malfunction.

performance of the system with an undetected malfunction on the DC-side voltage sensor of SM 4. The output value of this sensor is zero after malfunctioning at $t=1\,\mathrm{s}$. The system is tested in a low insolation condition in which the PV unit produces 25 W at its MPP. Fig. 13(b) shows the experimental setup terminal voltage before and after the undetected malfunction. The output voltage has a nine-level pattern before $t=1\,\mathrm{s}$. The malfunction of this sensor results in an uncontrolled output terminal voltage. This voltage does not have a nine-level pattern anymore.

In addition to the output terminal voltage, the output current also becomes unstable after the undetected sensor malfunction. Fig. 14(b) shows the experimental result on how the current waveform loses its sinusoidal shape and eventually becomes unstable. As a result of this undetected malfunction, the direction of the real power flow changes towards the DC-side capacitors, as shown in Fig. 15(b). If the protection system does not shut down the converter, uncontrolled overcharge of capacitors can occur.

The next experimental scenario analyzes the performance of the system under the same sensor malfunction, but detected. The insolation level and all the other test conditions remain unchanged compared to the undetected malfunction scenario. At $t=1\,$ s, the DC-side voltage sensor of SM 4 is lost. This malfunction is detected by the detection algorithm and

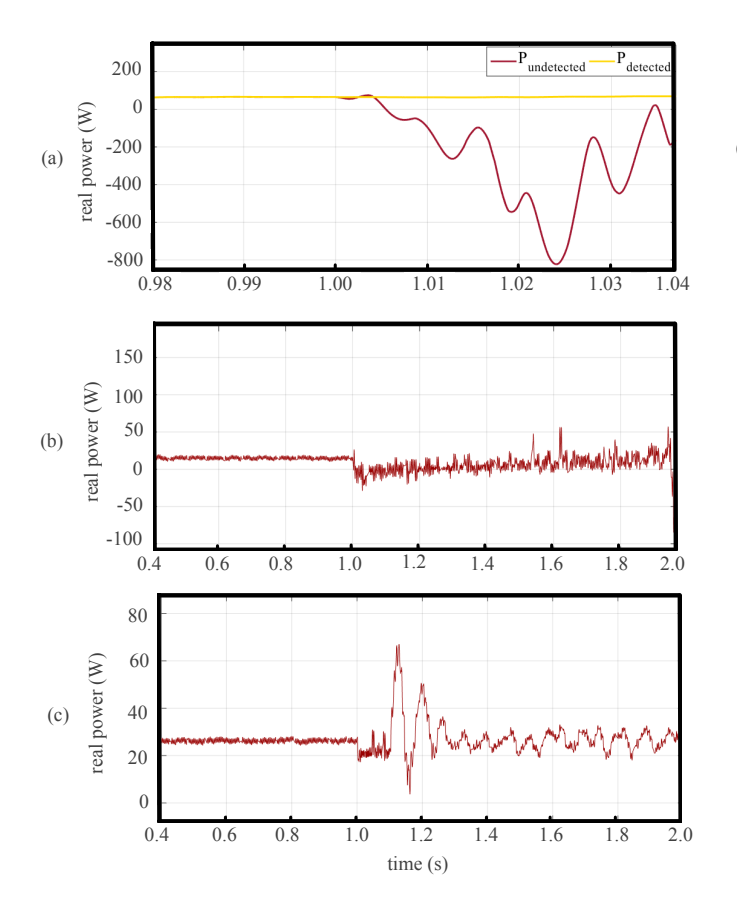


Fig. 15. Simulation ((a)) and experimental ((b),(c)) results for the output real power with a malfunction happening on V_{DC4} at $t=1.00~\rm s$, (a) comparison of a detected and an undetected malfunction in simulation, (b) experimental result for an undetected malfunction, and (c) experimental result for a detected malfunction.

the calculation replaces the measurement at t = 1.1 s. The estimate is able to keep the system operating normally after the malfunction of the sensor. Further, the MPPT algorithm is performed correctly before and after the malfunction. Fig. 13(c) shows the experimental result for the terminal voltage when a malfunction happens and is detected after 0.1 seconds. The voltage loses its nine-level sinusoidal pattern when the sensor malfunctions. However, replacing the measurement with the calculated value helps the system recover its nine-level terminal voltage. At t = 1.1 s, the terminal voltage goes back to its ninelevel pattern and the switching algorithm successfully tracks the reference value of the terminal voltage. Fig. 14(c) shows the AC-side current as a result of this detected malfunction in the experimental setup. The experimental results for the AC-side current and the real power, shown in Fig. 15(c), show that the system is able to maintain its stable and safe current and real power by replacing the wrong measurement by a calculated value. Figs. 16(a)-(d) show the experimental results for the DC-side output voltages of the sensors and their calculations in this scenario (detected malfunction). The actual value of the DC-side voltage for SM 4 is also shown after the malfunction of its sensor. Fig. 16(d) shows that the calculated value for SM 4 matches its actual DC-side voltage. Fig. 16(e) shows the experimental modulation index of SM 4 before and after

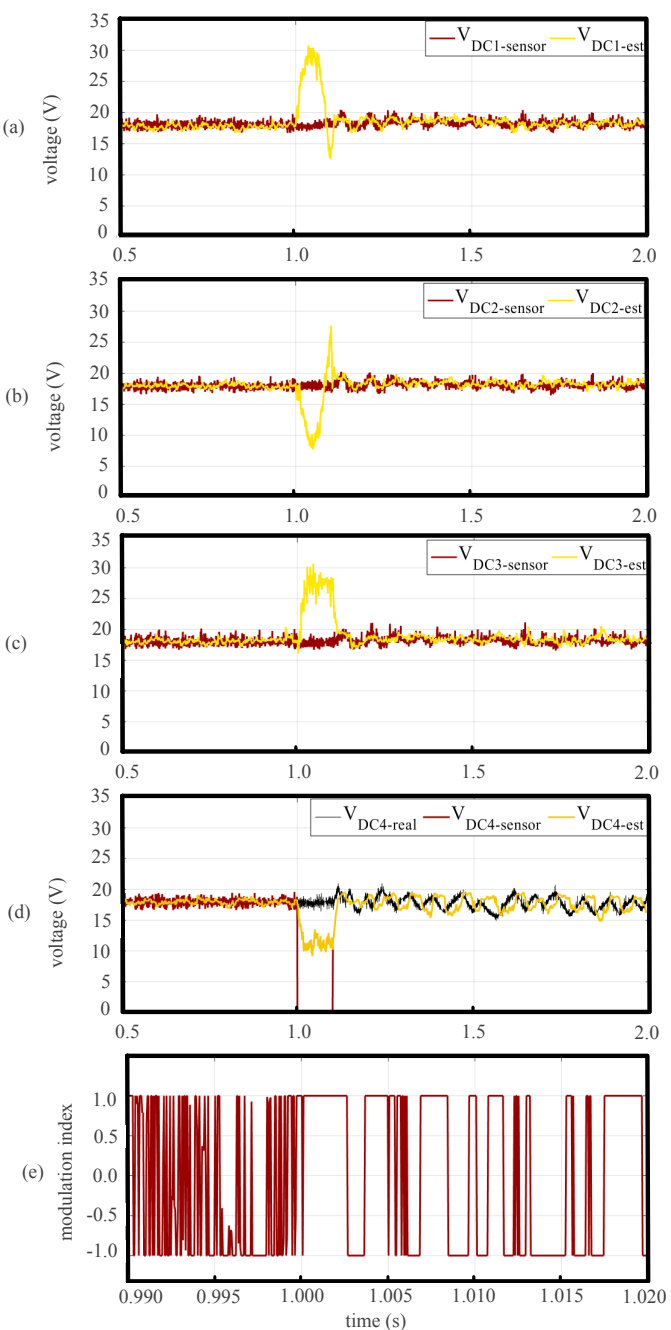


Fig. 16. Experimental results with a malfunction happening on V_{DC4} at $t=1.00\,\mathrm{s}$ (a)-(d) the outputs of the DC-side voltage sensors and their calculated values, (e) modulation index of SM 4.

the detection of the malfunction. Becuase SM 4 is detected to have a sensor malfunction on its DC side, at $t=1.00~\rm s$, its switching mode changes and it cannot work in PWM anymore. Fig. 16(d) shows V_{DC4} and how it remains well balanced when the switching policy changes and the SM does not work in PWM mode anymore.

VI. CONCLUSION

This paper proposes an algorithm to make a CHB-based PV system more resilient to sensor malfunctions. This resiliency

(i) reduces the concerns regarding the use of backup or highly expensive sensors; (ii) makes the system more reliable; and (iii) reduces the overall cost. This algorithm is based on estimating sensor measurements, detecting a malfunctioning sensor, and replacing the wrong measurement with an accurate calculation. The performance of the proposed algorithm is validated via both simulation and experimental studies on a nine-level CHB-based PV system. The proposed method can be generalized to an *n*-level CHB-based PV system. Although not studied in this paper, a similar, but simpler method can also be applied for half-bridge submodules.

REFERENCES

- I. E. Agency, "Tracking clean energy progress 2016: Energy technology perspectives 2016 excerpt, IEA input to the clean energy ministerial."
 [Online]. Available: http://www.iea.org/publications/freepublications/ publication/TrackingCleanEnergyProgress2016.pdf
- [2] S. E. I. Association, "U.S. solar market adds 2.4 gw in q2, largest second quarter ever." [Online]. Available: https://www.seia.org/news/ us-solar-market-adds-24-gw-q2-largest-second-quarter-ever
- [3] A. Teymouri, A. Mehrizi-Sani, and C. C. Liu, "Cyber security risk assessment of solar PV units with reactive power capability," in 44th IEEE Ind. Electron. Soc. Annu. Conf. (IECON), Oct. 2018.
- [4] P. Paganini, "Flaws in solar panels potentially threatening European power grids," 2017. [Online]. Available: http://securityaffairs.co/ wordpress/61750/hacking/solar-panels-flaws.html
- [5] A. Motley, "2017 solar eclipse report," 2017.[Online]. Available: https://www.caiso.com/Documents/Briefing_SolarEclipse-ISOReport-May_2017.pdf
- [6] CaliforniaISO, "August 21, 2017 solar eclipse review," 2017. [Online]. Available: https://www.caiso.com/Documents/SolarEclipse2017Review. pdf
- [7] A. Teymouri, S. H. Fathi, and G. B. Gharehpetian, "An advanced fuzzy control method to improve dynamic stability of power system with PV units," in 5th Int. Conf. Comp. Knowledge Eng. (ICCKE), Oct. 2015.
- [8] J. Chavarria, D. Biel, F. Guinjoan, C. Meza, and J. J. Negroni, "Energy-balance control of pv cascaded multilevel grid-connected inverters under level-shifted and phase-shifted pwms," *IEEE Trans. Ind. Electron.*, vol. 60, no. 1, pp. 98–111, Jan. 2013.
- [9] J. Sastry, P. Bakas, H. Kim, L. Wang, and A. Marinopoulos, "Evaluation of cascaded h-bridge inverter for utility-scale photovoltaic systems," *Renew. Energy*, vol. 69, pp. 208–218, Jan. 2014.
- [10] M. Miranbeigi and H. Iman-Eini, "Hybrid modulation technique for grid-connected cascaded photovoltaic systems," *IEEE Trans. Ind. Electron.*, vol. 63, no. 12, pp. 7843–7853, 2016.
- [11] C. D. Townsend, Y. Yu, G. Konstantinou, and V. G. Agelidis, "Cascaded h-bridge multilevel pv topology for alleviation of per-phase power imbalances and reduction of second harmonic voltage ripple," *IEEE Trans. Power Electron.*, vol. 31, no. 8, pp. 5574–5586, 2016.
- [12] Y. Yu, K. Georgios, C. Townsend, and V. Agelidis, "Comparison of zero-sequence injection methods in cascaded h-bridge multilevel converters for large-scale photovoltaic integration," *IET Renew. Power Gen.*, vol. 11, no. 5, pp. 603–613, 2016.
- [13] N. Sandeep and U. R. Yaragatti, "Design and implementation of a sensorless multilevel inverter with reduced part count," *IEEE Trans. Power Electron.*, vol. 32, no. 9, pp. 6677–6683, Jan. 2017.
- [14] M. D. Manjrekar, P. K. Steimer, and T. A. Lipo, "Hybrid multilevel power conversion system: A competitive solution for high-power applications," *IEEE Trans. Ind. Applicat.*, vol. 36, no. 3, pp. 834–841, Oct. 2000.
- [15] M. Veenstra and A. Rufer, "Control of a hybrid asymmetric multilevel inverter for competitive medium-voltage industrial drives," *IEEE Trans. Ind. Applicat.*, vol. 41, no. 2, pp. 655–664, Apr. 2005.
- [16] P. Rajeevan, K. Sivakumar, K. Gopakumar, C. Patel, and H. Abu-Rub, "A nine-level inverter topology for medium-voltage induction motor drive with open-end stator winding," *IEEE Trans. Ind. Electron.*, vol. 60, no. 9, pp. 3627–3636, Sept. 2013.
- [17] B. Yu and A. G. Abo-Khalil, "Current estimation based maximum power point tracker of grid connected pv system," in *Power Electron. Drive Systems (PEDS)*, 2013 IEEE 10th Int. Conf. IEEE, Apr. 2013, pp. 948–952.
- [18] N. Marks, T. Summers, and R. Betz, "Current sensorless maximum power point tracking in a cascaded h-bridge photovoltaic power system," in *Energy Conv. Cong. Exposition (ECCE)*, 2015 IEEE. IEEE, Sept. 2015, pp. 6461–6466.

- [19] J. Li, X. Peng, J. Wang, Q. Wang, Z. Lyu, and D. Zhang, "A current sensorless mppt algorithm for a low-cost pv array controller," in *Future Energy Electron. Conf. ECCE Asia (IFEEC 2017-ECCE Asia)*, 2017 IEEE 3rd Int. IEEE, Jun. 2017, pp. 728–732.
- [20] G. Escobar, S. Pettersson, C. Ho, M. Karppanen, and T. Pulli, "Pv current sensorless mppt for a single-phase pv inverter," in *IECON 2011-37th* Annu. Conf. IEEE Ind. Electron. Soc. IEEE, Nov. 2011, pp. 3906–3911.
- [21] G.-S. Seo, J.-W. Shin, B.-H. Cho, and K.-C. Lee, "Digitally controlled current sensorless photovoltaic micro-converter for dc distribution," *IEEE Trans. Ind. Informat.*, vol. 10, no. 1, pp. 117–126, Feb. 2014.
- [22] K. Itako and T. Mori, "A new current sensorless mppt control method for pv generation systems," in *Power Electron. Applicat.*, 2005 European Conf. IEEE, Sept. 2005, pp. 9–pp.
- [23] G. Farivar, B. Hredzak, and V. G. Agelidis, "A dc-side sensorless cascaded h-bridge multilevel converter-based photovoltaic system," *IEEE Trans. Ind. Electron.*, vol. 63, no. 7, pp. 4233–4241, July 2016.
- [24] Y.-H. Liao and C.-M. Lai, "Newly-constructed simplified single-phase multistring multilevel inverter topology for distributed energy resources," *IEEE Trans. Power Electron.*, vol. 26, no. 9, pp. 2386–2392, 2011.
- [25] K. K. Gupta, A. Ranjan, P. Bhatnagar, L. K. Sahu, and S. Jain, "Multilevel inverter topologies with reduced device count: A review," *IEEE Trans. Power Electron.*, vol. 31, no. 1, pp. 135–151, 2016.
- [26] P. Chaturvedi, S. Jain, and P. Agarwal, "Reduced switching loss pulse width modulation technique for three-level diode clamped inverter," *IET Power Electron.*, vol. 4, no. 4, pp. 393–399, Apr. 2011.
- [27] Y.-M. Park, H.-S. Yoo, H.-W. Lee, M.-G. Jung, S.-H. Lee, C.-D. Lee, S.-B. Lee, and J.-Y. Yoo, "A simple and reliable pwm synchronization & phase-shift method for cascaded h-bridge multilevel inverters based on a standard serial communication protocol," in *Ind. Applicat. Conf.*, 2006. 41st IAS Annu. Meeting. Conf. Record 2006 IEEE, vol. 2. IEEE, Oct. 2006, pp. 988–994.



Armin Teymouri (S'14) received his B.Sc. in electrical engineering from Ferdowsi University of Mashhad, Mashhad, Iran, in 2014. He got his M.Sc. in electrical engineering from Amirkabir University of Technology, Tehran, Iran, in 2016. He is currently working toward the Ph.D. degree at the School of Electrical Engineering and Computer Science, Washington State University, Pullman, WA, USA.

He is currently the Lead Power Electronics Engineer at Hyperloop One, Los Angeles, CA, USA. He was a Power Electronics Intern at WiTricity

Corporation, Boston, MA, USA, in 2019. He was an E-motor Control Intern with Mercedes-Benz Research and Development North America, Redford, MI, USA, in 2018. His areas of research interests include power electronics, electric vehicles, wide bandgap devices, wireless chargers, and smart grids.



Ali Mehrizi-Sani (S'05–GS'08–M'12–SM'15) received the B.Sc. degrees in electrical engineering and petroleum engineering from Sharif University of Technology, Tehran, Iran, both in 2005. He received the M.Sc. degree from the University of Manitoba, Winnipeg, MB, Canada, and the Ph.D. degree from the University of Toronto, Toronto, ON, Canada, both in electrical engineering, in 2007 and 2011.

He is currently an Associate Professor at Virginia Tech, Blacksburg, VA, USA, where he is Director of the Resilient Renewable Energy Grid Adaptation

Laboratory (REGAL). From 2012 to 2019, he was an Associate Professor and Assistant Professor at Washington State University, Pullman, WA. He has held Visiting Professor appointments at TU Graz, Graz, Austria, in 2014, 2016, and 2018. He was a Research Engineer with CanmeteNERGY, Montreal, QC, in 2019 and a Visiting Scientist with Manitoba Hydro International, Winnipeg, MB, in 2018. His areas of interest include power system applications of power electronics, integration of renewable energy resources, and low-inertia systems.

Dr. Mehrizi-Sani is an editor of IEEE TRANSACTIONS ON POWER SYSTEMS, IEEE TRANSACTIONS ON ENERGY CONVERSION, and IEEE POWER ENGINEERING LETTERS. He is a past editor of IEEE TRANSACTIONS ON POWER DELIVERY (2012–2019) and Wiley International Transactions on Electrical Energy Systems (ITEES) (2017–2019). He was the Chair of IEEE Task Force on Dynamic System Equivalents and the Secretary of CIGRE Working Group C4.34 on Application of PMUs for Monitoring Power System Dynamic Performance. He is the recipient of 2018 IEEE PES Outstanding Young Engineer Award, 2018 ASEE PNW Outstanding Teaching Award, 2017 IEEE Mac E. Van Valkenburg Early Career Teaching Award, 2017 WSU EECS Early Career Excellence in Research, 2016 WSU VCEA Reid Miller Excellence in Teaching Award, 2011 NSERC Postdoctoral Fellowship, and 2007 Dennis Woodford prize for his M.Sc. thesis. From 2007 to 2011, he was a Connaught Scholar at the University of Toronto.